

Bicontinuous oxide heteroepitaxy with enhanced photoconductivity

Received: 14 June 2022

Accepted: 29 November 2022

Published online: 03 January 2023

 Check for updates

Pao-Wen Shao¹, Yi-Xian Wu¹, Wei-Han Chen¹, Mojue Zhang², Minyi Dai², Yen-Chien Kuo³, Shang-Hsien Hsieh³, Yi-Cheng Tang⁴, Po-Liang Liu⁴, Pu Yu⁵, Yuang Chen⁶, Rong Huang⁶, Chia-Hao Chen³, Ju-Hung Hsu⁷, Yi-Chun Chen⁸, Jia-Mian Hu²  & Ying-Hao Chu^{1,9} 


Self-assembled systems have recently attracted extensive attention because they can display a wide range of phase morphologies in nanocomposites, providing a new arena to explore novel phenomena. Among these morphologies, a bicontinuous structure is highly desirable based on its high interface-to-volume ratio and 3D interconnectivity. A bicontinuous nickel oxide (NiO) and tin dioxide (SnO₂) heteroepitaxial nanocomposite is revealed here. By controlling their concentration, we fabricated tuneable self-assembled nanostructures from pillars to bicontinuous structures, as evidenced by TEM-energy-dispersive X-ray spectroscopy with a tortuous compositional distribution. The experimentally observed growth modes are consistent with predictions by first-principles calculations. Phase-field simulations are performed to understand 3D microstructure formation and extract key thermodynamic parameters for predicting microstructure morphologies in SnO₂:NiO nanocomposites of other concentrations. Furthermore, we demonstrate significantly enhanced photovoltaic properties in a bicontinuous SnO₂:NiO nanocomposite macroscopically and microscopically. This research shows a pathway to developing innovative solar cell and photodetector devices based on self-assembled oxides.

Composites outperforming the properties of constituents benefit from functional enhancement due to the addition of the second phase. Typically, desirable phases with designed dimensions and sizes are mixed in composite materials during the fabrication process. Thus, the acquisition of enhanced properties relies on the control of material distribution. This critical issue can be overcome via a thermodynamic approach based on the phase separation process. For example, the ideal microstructure for enhancing flux-pinning in high-temperature

superconductors was to introduce non-superconducting columnar defects within the oxide superconductors. Goyal et al. employed phase separation and strain-driven self-assembly to introduce self-assembled, vertical nanocolumns of insulating BaZrO₃ within YBCO, resulting in massive enhancement of flux-pinning^{1,2}. The original attention was given to the additional phase to tune the functionality of the primary phase, such as the modification of magnetotransport behaviors of (La,Ca)MnO₃ via the strain imposed by MgO³. Since then, this

¹Department of Materials Science and Engineering, National Yang Ming Chiao Tung University, Hsinchu 30010, Taiwan. ²Department of Materials Science and Engineering, University of Wisconsin-Madison, Madison, WI 53706, USA. ³National Synchrotron Radiation Research Center, Hsinchu 30076, Taiwan.

⁴Graduate Institute of Precision Engineering, National Chung Hsing University, Taichung 402, Taiwan. ⁵State Key Laboratory of Low Dimensional Quantum Physics and Department of Physics, Tsinghua University, 100084 Beijing, People's Republic of China. ⁶Key Laboratory of Polar Materials and Devices, Ministry of Education, East China Normal University, 200241 Shanghai, China. ⁷Integrated Service Technology, Hsinchu, Taiwan. ⁸Department of Physics, National Cheng Kung University, Tainan 70101, Taiwan. ⁹Department of Materials Science and Engineering, National Tsing Hua University, Hsinchu 30013, Taiwan.

 e-mail: jhu238@wisc.edu; yhchu@mx.nthu.edu.tw

approach of phase-separation and strain-driven self-assembly of vertical nanocolumns of one material within another has been used in various oxide and nitride systems and has also been referred to as vertically aligned nanocomposites^{4–11}. Because the strain states of the constituent phases remain independent of the thickness of the heterostructure, a research field based on this bottom-up methodology to obtain self-assembled vertical aligned nanocomposites (VANs) was formed to enhance the structural coupling⁴. An extensive exploration of strain-mediated systems has been carried out to acquire desired properties such as ferroelectricity and magnetic anisotropy⁵.

Later, the focus was placed on the coupling of two coexisting phases, resulting in enhanced studies on magnetoelectric nanocomposites^{6,7}. However, for current structures, especially in self-assembled oxide heteroepitaxy, one critical characteristic in these systems is the existence of a network composed of two different phases, with one as the major continuous matrix and the other as the isolated nanostructure, representing a classic structure attributed to the mechanism of nucleation and growth⁸. However, few works have focused on checkerboard Mn-doped CoFe_2O_4 ⁹ and nanomaze $(\text{La,Sr})\text{MnO}_3/\text{ZnO}$ heterostructures¹⁰. A bicontinuous heterostructure has only been observed in the isostructural system of TiO_2 and VO_2 ¹¹. However, such a microstructure is commonly seen in alloy and polymer systems. In metallurgy, a bicontinuous double percolated morphology can be obtained via spinodal decomposition^{12,13}, in which one thermodynamic phase spontaneously separates into two different phases. This differs from the traditional nucleation and growth process, where a nucleation barrier has to be overcome. In 2001, attention was given to nanoporosity after the selective dissolution of

electrochemically active elements. The resulting nanoporous sponge was suitable for catalytic and electrochemical applications¹². Moreover, in organic solar cells, the formation of bicontinuous phases, named bulk heterojunctions, significantly improves due to a dramatic increase in the interface area with strong charge interactions at the interface¹⁴. Thus, creating a bicontinuous heterostructure can enhance the charge interactions in oxide systems to boost the photovoltaic effects or photoconduction performance.

In this study, we propose a bottom-up approach to create a self-assembled oxide system with tuneable structural architectures (i.e., tortuous bicontinuous structure or isolated pillar structure) in epitaxial SnO_2/NiO nanocomposites. The reason for selecting the SnO_2/NiO system as the model system is (1) the structural similarity in rock salt NiO and rutile SnO_2 , in which the cations of both tin and nickel occupy octahedral sites. Moreover, they are both structurally compatible with sapphire substrates. (2) The SnO_2/NiO system reveals excellent potential in device applications such as photodetectors¹⁵, gas sensors^{16,17}, and photocatalysts¹⁸. In addition, the p/n junction in this system has been widely explored¹⁹. Therefore, the dominating interface characteristic of charge transport could be studied both macroscopically and microscopically.

Results

The details on growth can be found in the methods section. Structural analysis was conducted by X-ray diffraction (XRD) and transmission electron microscopy (TEM) to examine sample quality and determine the epitaxial relationship. Figure 1a displays typical X-ray scans of

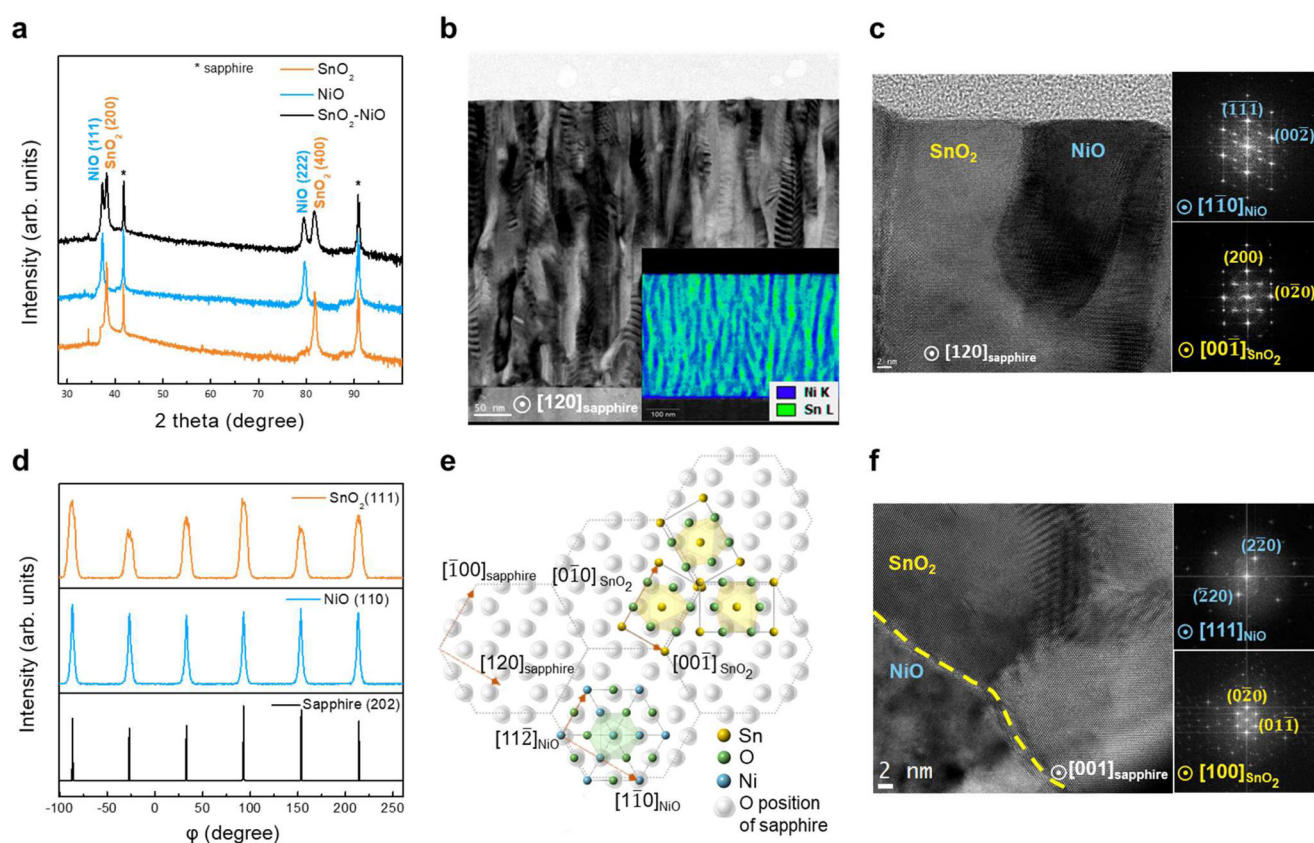


Fig. 1 | Bicontinuous nanostructures of $\text{SnO}_2/\text{NiO}/\text{sapphire}$ with a composition ratio of 1:1 (bicontinuous structure). a X-ray scans in theta–2theta mode of $\text{SnO}_2/\text{NiO}/\text{sapphire}$. **b** Cross-sectional TEM along the $[120]_{\text{sapphire}}$ zone axis. From top to bottom: surface, SnO_2/NiO , and sapphire. The inset shows the SEM–EDS elemental mapping at the same scale. The distribution of nickel and tin is combined in a layered image. **c** The larger scale of the cross-sectional HRTEM image along the $[120]_{\text{sapphire}}$ zone axis. Inset: FFT of NiO and SnO_2 . **d** In-plane phi-scan patterns of

sapphire (202) reflection, NiO (110) reflection, and SnO_2 (111) reflection. **e** Lattice projection along the epitaxial axis ($[400]_{\text{SnO}_2} \parallel [111]_{\text{NiO}} \parallel [001]_{\text{sapphire}}$). The orange arrows represent the in-plane orientation relationship. The projected positions of oxygen octahedra in SnO_2 and NiO overlap with that of sapphire. **f** Plane-view HRTEM image along the $[001]_{\text{sapphire}}$ zone axis. The yellow dotted line displays the boundary between NiO and SnO_2 . Inset: FFT of NiO and SnO_2 .

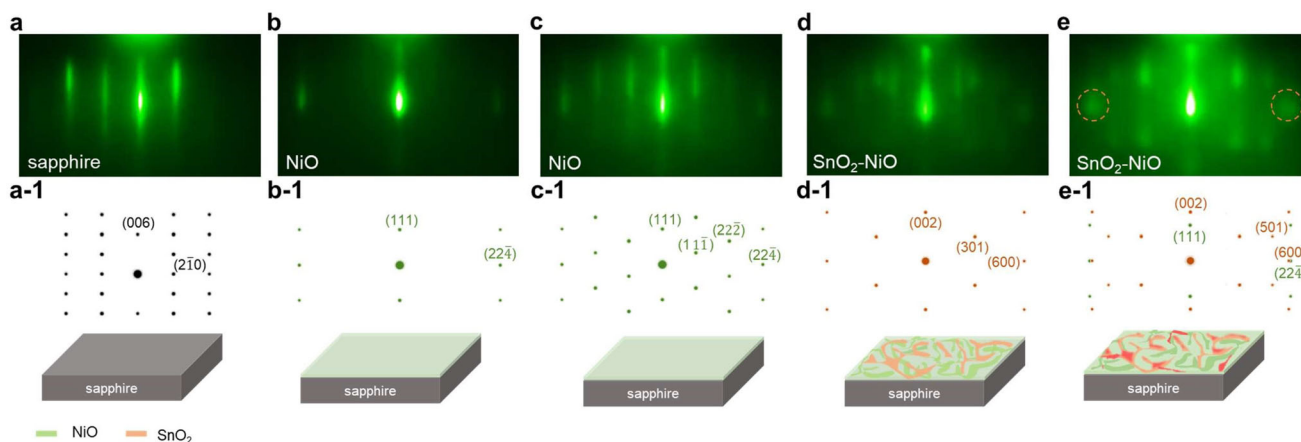


Fig. 2 | In situ RHEED patterns of the epitaxial growth of SnO₂:NiO on c-plane sapphire along $[120]_{\text{sapphire}}$ at 750 °C. **a** Initial state of c-plane sapphire. **a-1** The corresponding diffraction pattern of sapphire and schematics. **b–e** After 75, 125,

175, 225 pulses of deposition. **b1–e1** The corresponding diffraction patterns of NiO (green), SnO₂:NiO (orange), and schematics.

samples of SnO₂:NiO/sapphire, pure SnO₂/sapphire, and NiO/sapphire in θ - 2θ mode. Compared with the pure samples, the existence of both NiO(*111*) and SnO₂(*001*) diffraction peaks presents a single out-of-plane orientation of SnO₂:NiO/sapphire. Furthermore, X-ray rocking curves (Supplementary Fig. 1) display full-width at half-maximum (FWHM) values of 0.9° for NiO(*111*) and 1.2° for SnO₂(*200*), delivering evidence of the superior crystallinity of the heterostructure. After the annealing process (the details on the annealing conditions can be found in the Methods section), the cross-sectional TEM image (Fig. 1b) displays a pillar-like percolated feature of SnO₂:NiO/sapphire. STEM (Supplementary Fig. 2) and HRTEM images (Fig. 1c) further confirm that the termination of the NiO pillar is connected with SnO₂ rather than the substrate, representing a bicontinuous feature of SnO₂:NiO, which is further identified by X-ray energy-dispersive spectroscopy (EDS) with the compositional distribution of nickel and tin in the inset of Fig. 1b and Supplementary Fig. 2. Considering the disparate crystal structures of SnO₂ (rutile) and NiO (rock salt), this result shows the feasibility of bicontinuous features for self-assembled nanocomposites. In addition, the epitaxial relationship (i.e., $[100]_{\text{SnO}_2} \parallel [111]_{\text{NiO}} \parallel [001]_{\text{sapphire}}$, and $[001]_{\text{SnO}_2} \parallel [1\bar{1}0]_{\text{NiO}} \parallel [120]_{\text{sapphire}}$) of the self-assembled heteroepitaxial film is further characterized by larger-scale HRTEM (Fig. 1c) and the fast Fourier transform (FFT) in the inset. In addition, the HRTEM of a near edge-on SnO₂/NiO interface is not atomically sharp and flat (Supplementary Fig. 3), indicating that the tilt interface is beyond the epitaxial relationship, and bicontinuous features with various curved interfaces are expected.

Figure 1d reveals the XRD φ -scans of the SnO₂(*111*), NiO(*110*), and sapphire(*202*) reflections. For sapphire and NiO, there are six reflection peaks at every 60° interval, which is consistent with the sixfold symmetry of both NiO (cubic with two domains) along $[111]_{\text{NiO}}$ and sapphire (hexagonal) along the *c*-axis. Tetragonal SnO₂ is expected to display two reflection peaks at 180° intervals owing to twofold symmetry along $[100]_{\text{SnO}_2}$. However, it reveals six peaks at the same φ angles as those of NiO and sapphire. This result indicates that SnO₂ consists of three domains with a rotation of 120°, which are compatible with the sapphire substrate in Fig. 1e. Furthermore, for rutile SnO₂ and rock salt NiO, the projected positions of oxygen in octahedrons could overlap with those of oxygen in sapphire. In contrast, the projected positions of tin and nickel could coincide with that of aluminum in sapphire (Supplementary Fig. 4). Therefore, the heteroepitaxy of SnO₂:NiO/sapphire could be considered a continuous expansion of coherent hexagonal atomic arrangements, which is energetically favorable at the interface. Combined with the plane-view HRTEM and FFTs in Fig. 1f, the epitaxial relationship is further confirmed.

We further elaborate on the reason for forming SnO₂ and NiO phases instead of trigonal NiSnO₃. First, the fabrication temperature (i.e., 450–650 °C) for polycrystalline NiSnO₃ is similar to that of SnO₂ and NiO, ruling out inappropriate growth conditions²⁰. Second, NiSnO₃ displays trigonal crystal symmetry, yet the lattice misfit from the sapphire substrate is 2.6%²¹. Therefore, the projection position of oxygen in NiSnO₃ is similar to that of oxygen in sapphire, suggesting that the NiSnO₃ formation is not energetically favorable, likely due to the energy cost of the elastic deformation (in Supplementary Fig. 5).

Reflection high-energy electron diffraction (RHEED) was employed during the deposition of the SnO₂:NiO heterostructure to explore the initial growth dynamics and understand the phase separation process in real time. Figure 2a reveals the initial RHEED patterns of the c-plane sapphire substrate along $[120]_{\text{sapphire}}$, and the sharp striped pattern indicates a smooth and ordered surface. Figure 2a-1 reveals the corresponding diffraction pattern and the schematics of sapphire. Figure 2b, c were taken after 75 and 125 pulses, indicating striped patterns, which means that the initial stage of SnO₂:NiO deposition follows the Frank–van der Merwe growth mode (i.e., layer-by-layer growth). In addition, the diffraction patterns correspond to rock salt NiO (Fig. 2b-1, c-1), and we believe this is the initial unstable structure of the (Ni,Sn)O_x solid solution because the exact chemical composition (SnO₂:NiO) is transferred to the substrate during the deposition process. In addition, Fig. 2d, e reveal the RHEED patterns after 175 and 225 pulses of deposition, indicating the transition from the striped pattern to the spotty pattern. In contrast, the newly formed diffraction patterns in Fig. 2d correspond to rutile SnO₂ (*301*) (Fig. 2d-1). This phenomenon indicates that the subsequent deposition of SnO₂:NiO follows the Stranski–Krastanov (SK) growth mode (i.e., 2D to 3D growth). Moreover, the broad diffraction points in Fig. 2e (marked in orange dotted circles) could be explained by the close diffraction points of SnO₂ (*600*) and NiO (*224*) in Fig. 2e-1. This means that above the critical thickness, the rutile structure of SnO₂ precipitates from the unstable (Ni,Sn)O_x phase, which is further confirmed by the as-grown cross-sectional TEM (Supplementary Fig. 6). Therefore, the first decomposition occurs during the fabrication process. In contrast, the second decomposition occurs during the post-annealing process (as discussed in Fig. 3).

The rock salt structure tends to deposit first and is followed by precipitation of the rutile structure, which can be attributed to the differences in surface energy and shear modulus. To extend our understanding of this system, a series of density functional theory (DFT) simulations were performed to elucidate the interaction of atomic tin (nickel) with the NiO (SnO₂) surface. The results of the

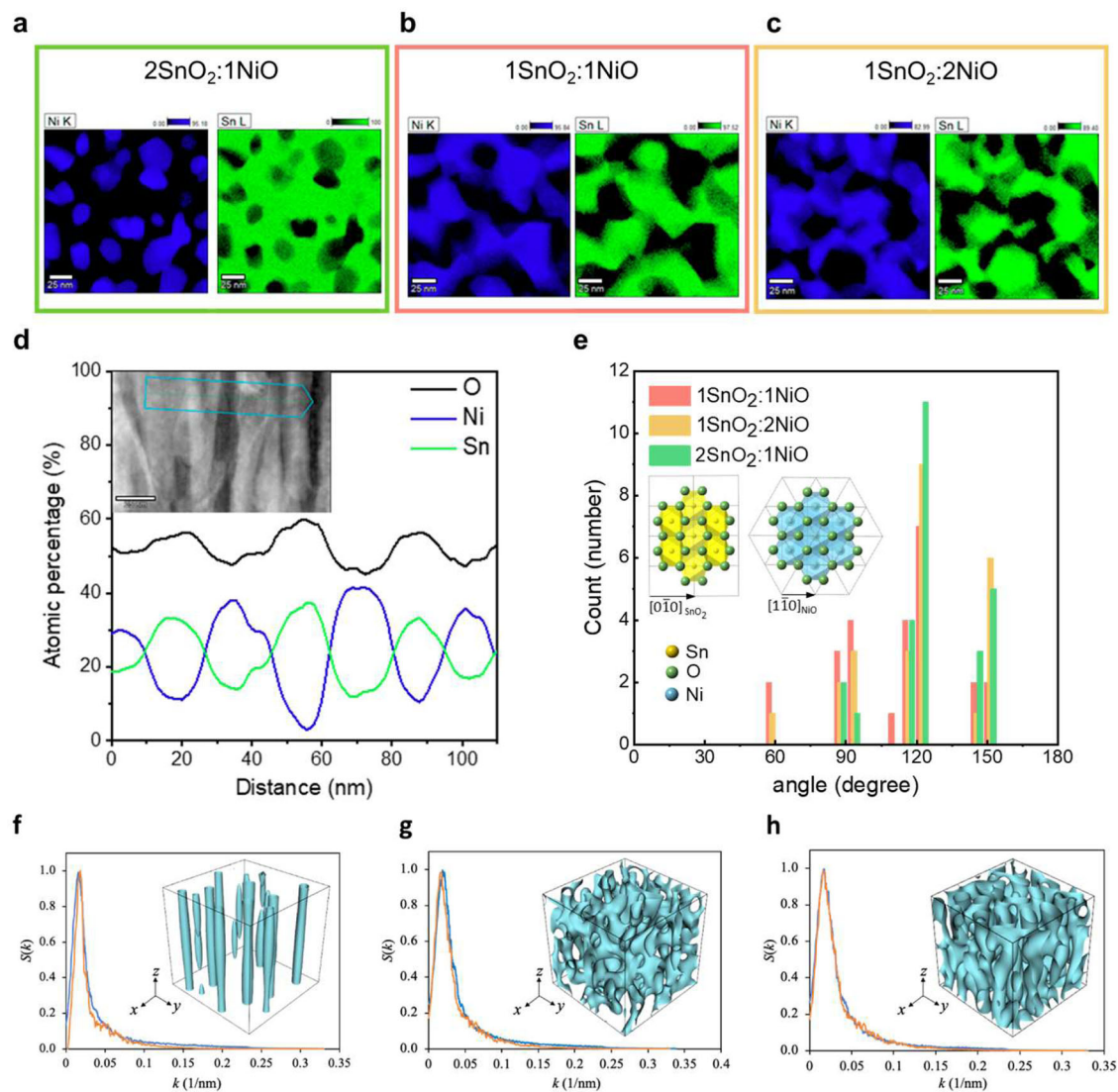


Fig. 3 | Experimental and estimated nanostructure of the $\text{SnO}_2\text{:NiO}$ system. Plane-view TEM-EDS element mapping of nickel (blue) and tin (green) of **a** $2\text{SnO}_2\text{:1NiO}$, **b** $\text{SnO}_2\text{:NiO}$, **c** $1\text{SnO}_2\text{:2NiO}$. **d** Compositional distribution of oxygen, nickel, and tin from the cross-sectional TEM image of the $\text{SnO}_2\text{:NiO}$ system with a composition ratio of 1:1 (bicontinuous) with the zone axis of $[120]_{\text{sapphire}}$. **e** Distribution of angles at each interface of **a-c**. Inset: projection of rutile SnO_2 and

rock salt NiO along the out-of-plane direction. **f-h**. Structure factor S as a function of wavenumber k for the microstructures of $2\text{SnO}_2\text{:1NiO}$, $\text{SnO}_2\text{:NiO}$, and $1\text{SnO}_2\text{:2NiO}$, respectively. The blue and orange curves were calculated based on their plane-view TEM images (Supplementary Fig. 8) and the 2D slice of the reconstructed 3D microstructures (shown in the insets, where the cyan color represents the morphology of the NiO phase; size: $256 \times 256 \times 256$ nm).

surface formation energies of $\text{Sn}_{\text{ad}}/\text{Ni}$ -terminated $\text{NiO}(111)$, $\text{Sn}_{\text{ad}}/\text{O}$ -terminated $\text{NiO}(111)$, $\text{Ni}_{\text{ad}}/\text{Sn}$ -terminated $\text{SnO}_2(100)$, and $\text{Ni}_{\text{ad}}/\text{O}$ -terminated $\text{SnO}_2(100)$ models are described in Supplementary Fig. 7, showing that $\text{Sn}_{\text{ad}}/\text{O}$ -terminated $\text{NiO}(111)$ has the lowest overall energy, even with negative surface energies at chemical potentials corresponding to $\Delta\mu_{\text{Sn}} = 0$ (Sn-rich) irrespective of the chemical potential condition of $\Delta\mu_{\text{Ni}}$. Note that our calculated surface energies of $\text{Sn}_{\text{ad}}/\text{O}$ -terminated $\text{NiO}(111)$ are $-0.06 \text{ eV}/\text{\AA}^2$ in the Sn-rich and Ni-rich limits, i.e., at $\Delta\mu_{\text{Sn}} = 0$ and $\Delta\mu_{\text{Ni}} = 0$, and $-0.13 \text{ eV}/\text{\AA}^2$ in the Sn-rich and O-rich limits, i.e., at $\Delta\mu_{\text{Sn}} = 0$ and $\Delta\mu_{\text{Ni}} = -1.13 \text{ eV}$. $\text{NiO}(111)$ has a low surface energy, representing preferential growth with the Frank-van der Merwe growth mode. When Sn atoms approach and adsorb on the $\text{NiO}(111)$ surface, the surface energy of $\text{NiO}(111)$ fluctuates, forming a negative surface energy; the $\text{NiO}(111)$ surface becomes rough, and the surface area increases. The driving force due to Sn atoms attaching to the $\text{NiO}(111)$ surface causes the nucleation to grow $\text{SnO}_2(100)$. Due to the high surface energy of $\text{SnO}_2(100)$ relative to the surface energy of $\text{NiO}(111)$, $\text{SnO}_2(100)$ is grown in three-dimensional (3D) islands in

heteroepitaxial growth with the SK growth mode. The surface energy fluctuation will break the crystal symmetry, resulting in surface-directed decomposition.

The determining factors of the morphology in the decomposition process include (a) the degree of compositional fluctuation; (b) the modulus mismatch and the crystal anisotropy between constituent phases; and (c) the lattice mismatch between the film and substrate²²⁻²⁸. First, as discussed in Fig. 2, $(\text{Ni,Sn})\text{O}_x$ is formed in a rock salt structure below the critical thickness, and SnO_2 with a rutile structure precipitates after reaching the required thickness, displaying the initial phase separation (i.e., first decomposition process) dominated by the lattice mismatch between the substrate and film and the surface energy difference between SnO_2 and NiO . Second, by controlling the $\text{SnO}_2\text{:NiO}$ content to be 2:1, 1:1, and 1:2, the degree of compositional fluctuation can be modulated. The decomposition in $\text{SnO}_2\text{:NiO}$ with pillar (Fig. 3a) and bicontinuous (Fig. 3b, c) microstructures could be observed after the postannealing process (i.e., second decomposition process) in the plane-view TEM-EDS with the

distribution of nickel and tin. During this procedure, the interface with a compositional gradient between the two phases migrates at the nanoscale, transforming from the as-grown SnO₂ precipitate (TEM in Supplementary Fig. 6) to pillar or bicontinuous textures (TEM in Supplementary Fig. 2). In addition, this bicontinuous structure represents multiple interfaces beyond the coherent relationship observed in X-ray diffraction, in which the termination of the NiO pillar is surrounded by adjacent SnO₂, ruling out a pure nucleation and growth mechanism. In addition, the magnified TEM image at the interface (Fig. 3d) with the compositional distribution of nickel and tin along the yellow arrow indicates the compositional gradient rather than a sharp interface. Moreover, these interfaces (Fig. 3a–c) display specific angles. As investigated by the edge detection and Hough transformed method in Supplementary Fig. 7, the angle dependence of interfaces is summarized in Fig. 3e, displaying high intensity at 60°, 90°, 120°, and 150°. This phenomenon indicates that the interface energy still modifies the second decomposition process, which the occupation site in oxides could estimate. The inset of Fig. 3e displays hexagons from the projection of both octahedrons. For rutile SnO₂ and rock salt NiO, tin and nickel occupy the octahedral sites surrounded by oxygen, indicating that both are coordinated to six oxygen atoms. However, they display, unlike crystal symmetry. Therefore, we believe that this similarity between structures and surface energy fluctuations provides a lower interface energy and dominates the phase separation process, resulting in a bicontinuous design with a specific angle of interfaces.

The thermodynamic driving force for phase separation is typically determined by reducing the local chemical free energy at the expense of the energy penalty from the interface (i.e., the interphase boundary) formation. For solid systems, long-range elastic interactions can also contribute significantly to the driving force. Despite such complexity, the key morphological features of the equilibrium microstructure are primarily dictated by the magnitudes and orientational anisotropy of the specific interface energies γ_i ($i = x, y, z$), where the subscript refers to the axis of the interface normal. This can be understood based on the well-known Wulff construction: a lower interface energy of a crystal leads to a shorter vector length at thermodynamic equilibrium. For example, the formation of vertical NiO pillars in the 2SnO₂:1NiO sample (Fig. 3a) suggests that γ_z is significantly larger than both γ_x and γ_y , and the pillars are more or less circular, indicating that $\gamma_x \approx \gamma_y$. Furthermore, the number of NiO pillars is related to the magnitude of γ_x and γ_y ; more pillars tend to form in the case of smaller γ_x and γ_y . For the SnO₂:NiO and 1SnO₂:2NiO samples, one can likewise deduce that (1) $\gamma_x \approx \gamma_y$ since their microstructure patterns are essentially symmetric along x and y , as seen from their plane-view TEM images (Supplementary Fig. 9e, h); (2) γ_z is more significant than γ_x and γ_y due to the preferred phase alignment along z , as shown by the cross-sectional TEM image (see Supplementary Fig. 2). Informed by these TEM images and the proposed phase diagram (Fig. 3d), we performed phase-field simulations to reconstruct the 3D microstructure of the 2SnO₂:1NiO, SnO₂:NiO, and 1SnO₂:2NiO nanocomposites (see Methods). As shown in Fig. 3f–h, the reconstructed microstructure is statistically equivalent to the 2D TEM images at all three NiO concentrations. Such reconstruction allows us to quantify the interface energy anisotropy for the SnO₂-NiO system and extract key thermodynamic parameters for predicting the microstructure morphologies of SnO₂-NiO nanocomposites of other NiO concentrations as well as similar oxide nanocomposites. Details are discussed in Supplementary Note 1.

After a detailed exploration of the structure, attention is given to charge interactions at the interface. The photoelectric conversion process includes light absorption, photocarrier generation, photocarrier transportation, and photocarrier extraction. A heterostructure's photovoltaic and photoconductive responses are typically enhanced by forming a p-n junction with proper band alignment. The effective interaction depends on the carrier concentration of p-type and n-type materials, creating a depletion region. The advantage of

such a bicontinuous structure is the formation of depletion regions in the whole sample, and the control of thickness can achieve optimized light absorption. The composition and thickness can be two independent factors for optimization; unlike a p-n junction in the bilayer structure, they are coupled. Therefore, with the p-n heterojunction and a high interface-to-volume ratio, the bicontinuous structure of SnO₂:NiO holds the advantage and potential to display a prominent photocurrent (i.e., photovoltaic effect). First, the bandgaps of SnO₂ and NiO are estimated to be 4.10 eV and 3.79 eV based on the spectra of optical absorption and the extrapolation from the Tauc method in the inset of Fig. 4a, indicating that the SnO₂:NiO heterostructure could absorb near UV illumination. Second, the band diagram of SnO₂:NiO could be characterized by a combination of the valance band maximum and the binding energy extracted from X-ray photoelectron spectroscopy (Supplementary Fig. 11) and bandgap analysis, as summarized in Fig. 4b. Due to the band bending in the type-II heterostructure, the photogenerated electrons would accumulate at SnO₂. At the same time, the holes would assemble at NiO. In addition, the depletion region was calculated to be ~29.8 nm (in Supplementary Note 2), which is comparable to the domain size in a bicontinuous structure (Fig. 3a–c). Therefore, an efficient carrier transport path could be expected regardless of the film thickness with a high interface-to-volume ratio. In Fig. 4c, the photovoltaic effect of the SnO₂/NiO bilayer, as well as the pillar and bicontinuous textures of self-assembled SnO₂:NiO, could be detected under the illumination of UV light with a wavelength of 265 nm, whose photon energy is more significant than the bandgaps of SnO₂ and NiO. The nonlinear photocurrent–voltage relationship (in Supplementary Fig. 12) reveals Schottky contact with a breakdown voltage of 26 V, representing typical photodiode behavior. Therefore, the depletion region and photocurrent could be modulated by transverse bias, and the responsivity (R) and detectivity (D) could be calculated by the following equations:

$$R = \frac{J_{\text{light}} - J_{\text{dark}}}{P_{\text{in}}} \quad (1)$$

$$D^* \cong \frac{R}{\sqrt{2qI_{\text{dark}}}} \quad (2)$$

J_{light} , J_{dark} , P , and q represent the photocurrent density ($\text{A} \times \text{cm}^{-2}$), dark current ($\text{A} \times \text{cm}^{-2}$), photo intensity (W/cm^2), and elementary charge (i.e., $1.602 \times 10^{-19} \text{C}$), respectively. As shown in Fig. 4c, the bilayer structure displays the lowest responsivity at each bias. In contrast, 1SnO₂:2NiO with a bicontinuous structure reaches a maximum responsivity of 2 A/W at a 10 V bias, and the detectivity reaches 10^{11} Jones, indicating that the photoactive heterojunction holds immense potential for photodetectors. On the other hand, we can obtain an adequate thickness of light absorption to enhance performance, which is determined to be 250 nm (discussed in Supplementary Fig. 13). In addition, the wavelength (i.e., domain size) of the bicontinuous SnO₂:NiO system is comparable to the depletion length calculated from the Hall effect measurement in Supplementary Note 2, which implies that the depletion region extends through the whole thin film, explaining why the bicontinuous structure displays higher responsivity than the bilayer structure.

The photoconductive response reveals that the interface-to-volume ratio of SnO₂:NiO dominates the current transport mechanism. Therefore, photocurrent detection through the AFM technique could build a close relationship between the photocurrent and the nanocomposite microstructure. Figure 4d demonstrates the schematic diagram of the measurement. An external laser illumination source with a wavelength of 405 nm was installed with a commercial AFM system, and the current was collected under a 10 V sample bias.

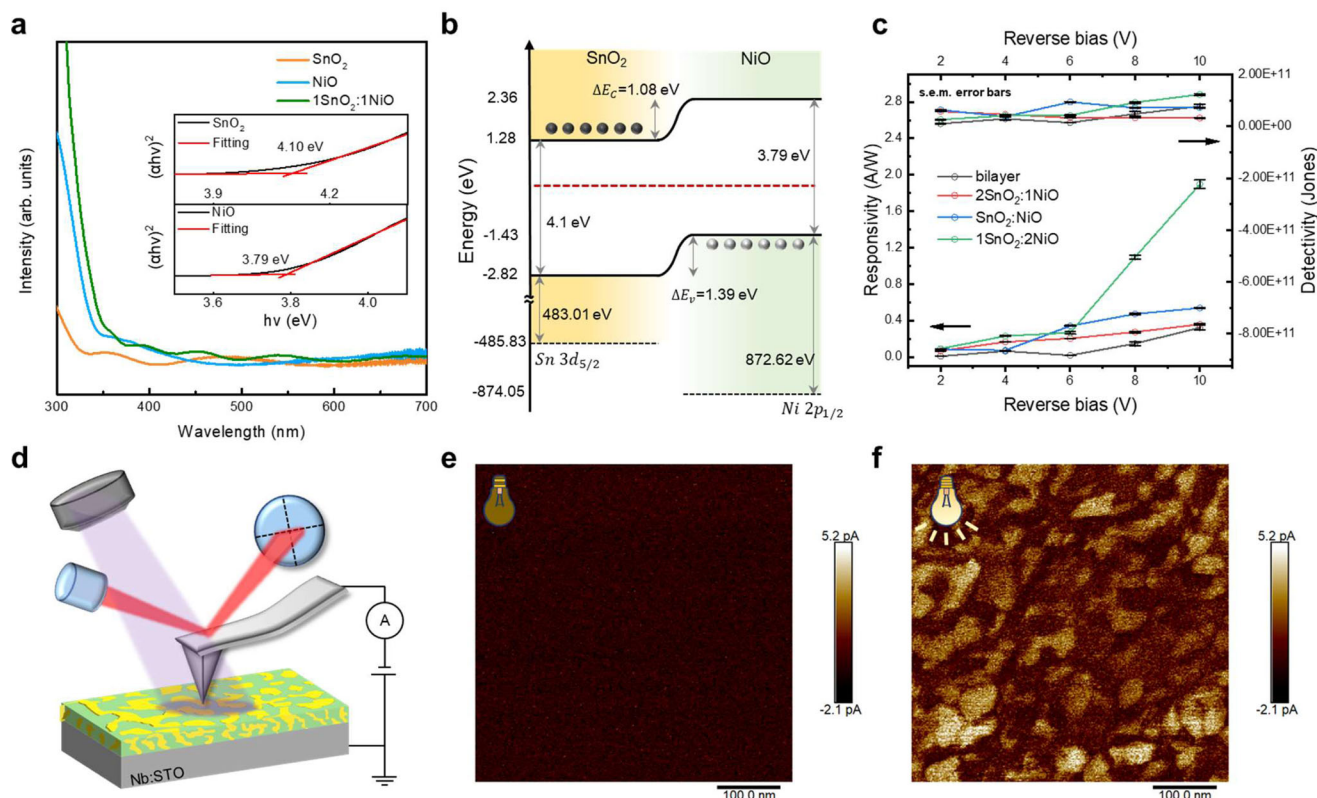


Fig. 4 | Band structure and photovoltaic properties of SnO₂:NiO. **a** The absorption spectra of SnO₂, NiO, and SnO₂:NiO. Inset: bandgap estimated from the Tauc method. **b** Band diagram estimated by XAS, XPS, and absorption spectrum. **c** Photovoltaic response of annealed SnO₂:NiO with a composition ratio of 2:1 (pillar), 1:1 (bicontinuous), 1:2 (bicontinuous), and bilayer SnO₂/NiO. **d** Illustration of

photoconductive AFM on a SnO₂:NiO/Nb:STO thin film with a composition ratio of 1:1 (bicontinuous). The external laser source with a 405 nm wavelength is coconstructed with a commercial AFM system. **e** Dark current, and **f** photocurrent of the SnO₂:NiO/Nb:STO thin film under a 10 V sample bias.

Compared with the dark current in Fig. 4e with the same scale, the photocurrent as imaged in Fig. 4f displays a significant photocurrent with the bicontinuous feature, which could be compared with the plane-view TEM with the self-organized feature in Supplementary Fig. 14. In addition, the higher photocurrent area is expected to be a SnO₂-rich region due to the higher mobility and higher carrier concentration^{29,30}. Therefore, based on the photovoltaic and localized photocurrent distribution analysis, the self-assembled structure with more extensive regions of p-n interfaces displays higher responsivity and detectivity, delivering promising evidence of the strong charge interaction of the bicontinuous structure.

Discussion

This study demonstrates a self-assembled oxide with a bicontinuous structure in the SnO₂:NiO system. The in situ growth mechanism was monitored by RHEED, indicating that a rock salt structure with a minor misfit formed initially and then was followed by the precipitation of a rutile structure with a more significant misfit. In addition, decomposition occurred during the annealing process. XRD and TEM have identified the epitaxial relationship, while the elemental distribution of Sn and Ni reveals a bicontinuous structure with a specific angle-dependent interface. Although rutile SnO₂ and rock salt NiO display different crystal symmetry and oxidation states, we suggest the bicontinuous form because their similar projected octahedral frameworks could be considered a continuous expansion of coherent hexagonal atomic arrangements in sapphire. Benefiting from a higher interface-to-volume ratio, the photovoltaic activity of the bicontinuous structure is more potent than that of the bilayer structure, revealing the advantage of a tortuous three-dimensional nanocomposite with strong charge interactions. This

work displays a double-percolated system with a distinct structure in oxide systems. This expands the practical application of self-assembled oxide systems through well-designed electronic interfaces in VANs.

Methods

Sample preparation and annealing process

The SnO₂:NiO/sapphire, SnO₂/sapphire, and NiO/sapphire thin film was fabricated via pulsed laser deposition³¹ with commercial SnO₂:NiO (SnO₂: NiO = 1:1, 1:2, 2:1), SnO₂, NiO, and ITO (90% In₂O₃ and 10% SnO₂) targets (ITO is for a top electrode in photo-voltaic analysis). Commercial c-sapphire was used as the substrate. Before the deposition process, the vacuum chamber was evacuated to a base pressure of 1×10^{-5} Torr. SnO₂ was deposited at 3 mTorr, and the substrate was heated to 750 °C, while NiO was grown under the same atmosphere, and the substrate was cooled down to 550 °C. The growth of SnO₂:NiO was carried out at 8 mTorr with a substrate temperature of 750 °C. Lastly, ITO top electrode (30 nm) was deposited by RF sputtering at 0.3 mTorr with an Ar flow of 20 sccm under room temperature. The RF power was controlled at 175 W. The annealing process is operated at 900 °C for 6 hrs, followed by the cooling rate of 0.4 °C/s. The thickness of the thin film is ~250 nm.

X-ray diffraction and absorption spectrum

XRD investigation was carried out by Bruker D2 Discover XRD System with Cu K_α x-ray ($\lambda = 1.5406 \text{ \AA}$) to acquire the 2θ - θ scan along a normal direction. φ scans and rocking curve measurements were acquired using a D8 advance XRD (Bruker). The optical absorbance of the heterostructure was measured by a commercial PerkinElmer Lambda-900 spectrometer.

Electron microscopy characterization and analysis

The specimen was prepared by focused ion beam (FEI Helios NanoLab 660) for TEM analyses. The ion-beam source's resolution can reach 4 nm at 30KV accelerating voltage. The information of HRTEM and STEM-EDS were acquired at room temperature on (JEOL JEM-2800F) with 200KV accelerating voltage. The TEM and STEM resolutions were 0.1 nm and 0.2 nm, respectively.

First-principles DFT calculations

We studied the surface formation energy of atomic tin with Ni- and O-terminated NiO(111) and atomic nickel with Sn- and O-terminated SnO₂(100) by first-principles DFT calculations with general gradient approximation (GGA) functional PW91^{32,33}, implemented in the Vienna ab initio simulation package (VASP) code^{34–36}. The electronic configurations for valence electrons are O 2s²2p⁴, and Ni 4s²3d⁸, and Sn 5s²5p². The converged slab geometries of one tin (nickel) atom on the Ni- and O-terminated NiO(111) (Sn- and O-terminated SnO₂(100)) separated by a vacuum region equivalent to a thickness of 40 Å, i.e., Sn_{ad}/Ni-terminated NiO(111), Sn_{ad}/O-terminated NiO(111), Ni_{ad}/Sn-terminated SnO₂(100), and Ni_{ad}/O-terminated SnO₂(100) models, were constructed using bulk crystalline configurations. The surface formation energy σ is defined as the excess energy on the surface of a slab compared with the bulk, namely, $\sigma = (E_{\text{slab}} - \sum n_i \mu_i) / 2A$, where E_{slab} is the total energy of the slabs with repeated geometry. n_i and μ_i are the numbers of atoms and chemical potentials of the constituents of the slab, respectively. A is the surface area. The chemical potential of Ni is restricted within the thermodynamically allowed ranges as follows: $\mu_{\text{Ni}}^{\text{bulk}} + \Delta H^f [\text{NiO}] \leq \mu_{\text{Ni}} \leq \mu_{\text{Ni}}^{\text{bulk}}$, i.e. $\Delta H^f [\text{NiO}] \leq \mu_{\text{Ni}} - \mu_{\text{Ni}}^{\text{bulk}} \leq 0$ or simply $\Delta H^f [\text{NiO}] \leq \Delta \mu_{\text{Ni}} \leq 0$, the chemical potential of Sn is restricted within the thermodynamically allowed ranges as follows: $\mu_{\text{Sn}}^{\text{bulk}} + \Delta H^f [\text{SnO}_2] \leq \mu_{\text{Sn}} \leq \mu_{\text{Sn}}^{\text{bulk}}$, i.e. $\Delta H^f [\text{SnO}_2] \leq \mu_{\text{Sn}} - \mu_{\text{Sn}}^{\text{bulk}} \leq 0$ or simply $\Delta H^f [\text{SnO}_2] \leq \Delta \mu_{\text{Sn}} \leq 0$. Our formation enthalpy of bulk NiO and SnO₂, $\Delta H^f [\text{NiO}]$ and $\Delta H^f [\text{SnO}_2]$, is determined from the total energies per atom of bulk NiO (space group: 225 *Fm-3m*) and bulk SnO₂ (space group: 136 *P4₂/mmm*), respectively, yielding $\Delta H^f [\text{NiO}] = -1.13$ eV and $\Delta H^f [\text{SnO}_2] = -5.30$ eV, in excellent agreement with other calculated value of $\Delta H^f [\text{SnO}_2] = -5.90$ eV³⁷.

Phase-field simulations

The equilibrium phase morphologies of the self-assembled SnO₂-NiO nanocomposite films were simulated using a 3D phase-field model of phase separation³⁸ implemented in the μ -Pro[®] software package. Both kinetic pathways of phase separation: nucleation and growth, and near-spinodal decomposition are considered depending on the concentration of NiO. Each microstructure is described using the 3D spatial distribution of the concentration of NiO (c_{NiO}) in the two-phase mixture. The equilibrium distribution of c_{NiO} was obtained by numerically solving the Cahn-Hilliard equation without a priori assumption on the microstructure patterns. 2D Fast Fourier Transformation is performed to extract the feature lengths of the two-phase microstructure from each 2D slice of the 3D microstructure pattern for comparison to those extracted the same way from the TEM images. Details of the phase-field simulations and feature-length extraction are provided in Supplementary Note 1.

Photo-conductive atomic force microscopy

Photo-conductive atomic force microscopy was carried out on a commercial SPM system (Bruker MultiMode 8 SPM system) with the combination of the light source of a 405 nm laser pointer. Diamond tips (Adama AD-40-AS, resonance frequency = 200 kHz) were used for photo-current detection.

Photo-voltaic measurement

To conduct the photovoltaic measurement, the ITO top circular electrode (radius = 100 μm) was deposited via a mask by RF

sputtering, and the bottom electrode was further connected to form a circuit. When applying bias, to remain within the reverse bias region, 80 nm of NiO (p-type) thin film was deposited above the bicontinuous and pillar structure of the SnO₂-NiO system. The dark and photocurrent measurements were carried out by a semiconductor analyzer (Keithley 4200 and Keysight B1500a) with the combination of a light source under a wavelength of 265 nm and an energy density of 0.375 mW cm⁻², and the current density was obtained about the top electrode area ($\sim 3.14 \times 10^{-4}$ cm²).

Data availability

All data supporting the results of this study are available in the manuscript or the supplementary information. Additional data are available from the corresponding author upon request.

References

- Goyal, A. et al. Irradiation-free, columnar defects comprised of self-assembled nanodots and nanorods resulting in strongly enhanced flux-pinning in YBa₂Cu₃O_{7- δ} films. *Superconductor Sci. Technol.* **18**, 1533–1538 (2005).
- Wee, S. H. et al. Self-assembly of nanostructured, complex, multi-cation films via spontaneous phase separation and strain-driven ordering. *Adv. Funct. Mater.* **23**, 1912–1918 (2013).
- Moshnyaga, V. et al. Structural phase transition at the percolation threshold in epitaxial (La_{0.7}Ca_{0.3}MnO₃)_{1-x}:(MgO)_x nanocomposite films. *Nat. Mater.* **2**, 247–252 (2003).
- Zhang, W., Ramesh, R., MacManus-Driscoll, J. L. & Wang, H. Multifunctional, self-assembled oxide nanocomposite thin films and devices. *MRS Bull.* **40**, 736–745 (2015).
- Huang, J., MacManus-Driscoll, J. L. & Wang, H. New epitaxy paradigm in epitaxial self-assembled oxide vertically aligned nanocomposite thin films. *J. Mater. Res.* **32**, 4054–4066 (2017).
- Yildiz, A., Tomishige, M., Vale, R. D. & Selvin, P. R. Kinesin walks hand-over-hand. *Science* **303**, 676–678 (2004).
- Zavaliche, F. et al. Electric field-induced magnetization switching in epitaxial columnar nanostructures. *Nano Lett.* **5**, 1793–1796 (2005).
- MacManus-Driscoll, J. L. Self-assembled heteroepitaxial oxide nanocomposite thin film structures: designing interface-induced functionality in electronic materials. *Adv. Funct. Mater.* **20**, 2035–2045 (2010).
- Ni, Y. & Khachatryan, A. G. From chessboard tweed to chessboard nanowire structure during pseudospinodal decomposition. *Nat. Mater.* **8**, 410–414 (2009).
- Chen, A. et al. Magnetotransport properties of quasi-one-dimensionally channeled vertically aligned heteroepitaxial nanomazes. *Appl. Phys. Lett.* **102**, 093114 (2013).
- Hiroi, Z. et al. Spinodal decomposition in the TiO₂-VO₂ system. *Chem. Mater.* **25**, 2202–2210 (2013).
- Erlebacher, J., Aziz, M. J., Karma, A., Dimitrov, N. & Sieradzki, K. Evolution of nanoporosity in dealloying. *Nature* **410**, 450–453 (2001).
- Derby, B. K., Chatterjee, A. & Misra, A. Metal-ion-controlled growth and nanoindentation response of 3D, bicontinuous Cu-Fe thin films. *J. Appl. Phys.* **128**, 035303 (2020).
- Crossland, E. J. W. et al. A bicontinuous double gyroid hybrid solar cell. *Nano Lett.* **9**, 2807–2812 (2009).
- Long, Z. et al. Cross-Bar SnO₂-NiO nanofiber-array-based transparent photodetectors with high detectivity. *Adv. Electron Mater.* **6**, 1901048 (2020).
- Hidalgo, P., Castro, R. H. R., Coelho, A. C. V. & Gouvêa, D. Surface segregation and consequent SO₂ sensor response in SnO₂-NiO. *Chem. Mater.* **17**, 4149–4153 (2005).
- Lv, P. et al. Study on a micro-gas sensor with SnO₂-NiO sensitive film for indoor formaldehyde detection. *Sens. Actuat. B: Chem.* **132**, 74–80 (2008).

18. Suvith, V. S., Devu, V. S. & Philip, D. Facile synthesis of SnO₂/NiO nano-composites: structural, magnetic and catalytic properties. *Ceram. Int.* **46**, 786–794 (2020).
 19. Maarisetty, D. & Baral, S. S. Effect of defects on optical, electronic, and interface properties of NiO/SnO₂ heterostructures: dual-functional solar photocatalytic H₂ production and RhB degradation. *ACS Appl Mater. Interfaces* **13**, 60002–60017 (2021).
 20. Yude, W., Xiaodan, S., Yanfeng, L., Zhenlai, Z. & Xinghui, W. Perovskite-type NiSnO₃ used as the ethanol sensitive material. *Solid-State Electron.* **44**, 2009–2014 (2000).
 21. Jain, A. et al. The Materials Project: a materials genome approach to accelerating materials innovation. *APL Mater.* **1**, 011002 (2013).
 22. Seol, D. J. et al. Computer simulation of spinodal decomposition in constrained films. *Acta Mater.* **51**, 5173–5185 (2003).
 23. Povstugar, I., Choi, P.-P., Tytko, D., Ahn, J.-P. & Raabe, D. Interface-directed spinodal decomposition in TiAlN/CrN multilayer hard coatings studied by atom probe tomography. *Acta Mater.* **61**, 7534–7542 (2013).
 24. Tang, M. & Karma, A. Surface modes of coherent spinodal decomposition. *Phys. Rev. Lett.* **108**, 265701 (2012).
 25. Bastea, S., Puri, S. & Lebowitz, J. L. Surface-directed spinodal decomposition in binary fluid mixtures. *Phys. Rev. E* **63**, 041513 (2001).
 26. Vaynzof, Y. et al. Surface-directed spinodal decomposition in poly[3-hexylthiophene] and C61-butyric acid methyl ester blends. *ACS Nano* **5**, 329–336 (2011).
 27. Jones, R. A. L., Norton, L. J., Kramer, E. J., Bates, F. S. & Wiltzius, P. Surface-directed spinodal decomposition. *Phys. Rev. Lett.* **66**, 1326–1329 (1991).
 28. Puri, S. Surface-directed spinodal decomposition. *J. Phys.: Condens. Matter* **17**, R101–R142 (2005).
 29. Shan, F. et al. High-mobility p-type NiO_x thin-film transistors processed at low temperatures with Al₂O₃ high-k dielectric. *J. Mater. Chem. C* **4**, 9438–9444 (2016).
 30. Mun, H., Yang, H., Park, J., Ju, C. & Char, K. High electron mobility in epitaxial SnO_{2-x} in semiconducting regime. *APL Mater.* **3**, 076107 (2015).
 31. Huang, Y.-L. et al. Pulsed laser deposition of complex oxide heteroepitaxy. *Chin. J. Phys.* **60**, 481–501 (2019).
 32. Kresse, G. & Joubert, D. From ultrasoft pseudopotentials to the projector augmented-wave method. *Phys. Rev. B* **59**, 1758–1775 (1999).
 33. Perdew, J. P. et al. Atoms, molecules, solids, and surfaces: applications of the generalized gradient approximation for exchange and correlation. *Phys. Rev. B* **46**, 6671–6687 (1992).
 34. Kresse, G. & Furthmüller, J. Efficient iterative schemes for ab initio total-energy calculations using a plane-wave basis set. *Phys. Rev. B* **54**, 11169–11186 (1996).
 35. Kresse, G. & Furthmüller, J. Efficiency of ab-initio total energy calculations for metals and semiconductors using a plane-wave basis set. *Comput. Mater. Sci.* **6**, 15–50 (1996).
 36. Kresse, G. & Hafner, J. Norm-conserving and ultrasoft pseudopotentials for first-row and transition elements. *J. Phys. Condens. Matter* **6**, 8245–8257 (1994).
 37. Liu, S., Liu, L., Cheng, Z., Zhu, J. & Yu, R. Atomic structure and properties of SnO₂ (100) and (101) surfaces and (301) steps in the (100) surface. *J. Phys. Chem. C* **124**, 27631–27636 (2020).
 38. Hu, J.-M. et al. Phase-field based multiscale modeling of heterogeneous solid electrolytes: applications to nanoporous Li₃PS₄. *ACS Appl. Mater. Interfaces* **9**, 33341–33350 (2017).
- MOST 109-2634-F-009-028, MOST 106-2112-M-001-036-MY3, and MOST 109-2112-M-001-043-MY3) and the Center for Emergent Functional Matter Science of National Chiao Tung University from The Featured Areas Research Center Program within the framework of the Higher Education Sprout Project by the Ministry of Education (MOE) in Taiwan. The work at University of Wisconsin-Madison was supported by the NSF award CBET-2006028 and the American Chemical Society Petroleum Research Fund under the award PRF #61594-DNI9. The phase-field simulations were performed using Bridges at the Pittsburgh Supercomputing Center through allocation TG-DMR180076, which is part of the Extreme Science and Engineering Discovery Environment (XSEDE) and supported by NSF grant ACI-1548562.

Author contributions

P.W.S., Y.H.C., and J.M.H. designed the experiments. Y.X.W. and W.H.C. synthesized the films and conducted structural characterization and electrical analysis, including XRD, RHEED, and photoconductivity. P.W.S. and Y.C.C. performed the C-AFM analysis. M.Z. and M.D. performed the phase field simulation. Y.C.K., S.H.H., and C.H.C. completed the band structure analysis via XPS. Y.C.T., and P.L.L. conducted the DFT simulation. J.H.H. performed the TEM and EDS characterization. P.W.S. analyzed the angle of the interface. Y.X.W., W.H.C., M.Z., M.D., J.M.H., Y.C.T., P.L.L., Y.C., R.H., and J.H.H. contributed to the analysis and understanding of the data. P.W.S., Y.H.C., and J.M.H. wrote the core of the manuscript. P.L.L., P.Y., Y.C.C., Y.H.C., and J.M.H. supervised the research. All the authors contributed to the discussion and manuscript preparation and read the final manuscript.

Competing interests

The authors declare no competing interests.

Additional information

Supplementary information The online version contains supplementary material available at <https://doi.org/10.1038/s41467-022-35385-0>.

Correspondence and requests for materials should be addressed to Jia-Mian Hu or Ying-Hao Chu.

Peer review information *Nature Communications* thanks Xuejing Wang and the other, anonymous, reviewer(s) for their contribution to the peer review of this work.

Reprints and permissions information is available at <http://www.nature.com/reprints>

Publisher's note Springer Nature remains neutral with regard to jurisdictional claims in published maps and institutional affiliations.

Open Access This article is licensed under a Creative Commons Attribution 4.0 International License, which permits use, sharing, adaptation, distribution and reproduction in any medium or format, as long as you give appropriate credit to the original author(s) and the source, provide a link to the Creative Commons license, and indicate if changes were made. The images or other third party material in this article are included in the article's Creative Commons license, unless indicated otherwise in a credit line to the material. If material is not included in the article's Creative Commons license and your intended use is not permitted by statutory regulation or exceeds the permitted use, you will need to obtain permission directly from the copyright holder. To view a copy of this license, visit <http://creativecommons.org/licenses/by/4.0/>.

© The Author(s) 2023, corrected publication 2023

Acknowledgements

Ministry of Science and Technology supports this work, Taiwan (grant No. MOST 109-2124-M-009-009-, MOST 109-2124-M-009-001-MY3,